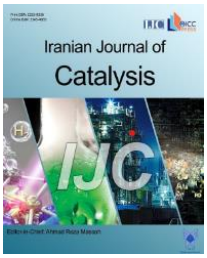

Iran. J. Catal. 2026; 16(2): 222-241

Iranian Journal of Catalysis (IJC)

https://doi.org/10.57647/ijc.2026.1602.15

Research Article

Vanadium-Doped Zirconia as an Efficient Visible-Light Photocatalyst for Advanced Treatment of Dye-Loaded Wastewater

Samra Tahir[1,*], Fatima Waheed[1], Momal Akram[2], Muhammad Salman[1], Umar Farooq[1], Saad Saleem[1], Amna Ehsan[1]

[1] *School of Chemistry, University of the Punjab, Lahore 54590, Pakistan*

[2] *Department of Basic & Applied Chemistry, Faculty of Science & Technology, University of Central Punjab, Lahore 54000, Pakistan*

[*] **Corresponding authors:** tahirsamra64@gmail.com

Article History:

Received:
22 October 2025

Revised:
30 November 2025

Accepted:
07 February 2026

Published Online:
08 May 2026

Published in Issue:
30 June 2026

© 2026 The Author(s). Published by the OICC Press under the terms of the CC BY 4.0, Creative Commons Attribution License, which permits use, distribution and reproduction in any medium, provided the original work is properly cited.

Abstract

The Vanadium oxide doped zirconia (V–ZrO_2) nanoparticles were synthesized via a wet-impregnation route and evaluated as visible-light photocatalysts for the degradation of malachite green (MG). Structural and surface analyses (XRD, FTIR, SEM–EDX, pHpzc) confirmed the formation of mixed-phase ZrO_2 with dispersed surface vanadium species that enhance light absorption and reduce band gap to ~2.2 eV. The photocatalytic performance was optimized by varying key operational parameters. The maximum degradation efficiency was obtained at pH 12, 0.3 g catalyst dose, 10 ppm initial dye concentration, 45 min irradiation, and 60 °C, achieving 95–97% MG removal. Kinetic analysis showed that the degradation followed the pseudo-second-order model (R^2 = 0.9645) more closely than the pseudo-first-order model (R^2 = 0.8521), supported by the Langmuir–Hinshelwood fit (R^2 = 0.99), indicating a surface-controlled, adsorption-dependent pathway. Temperature dependent kinetics yielded activation energies of 12.9 kJ·mol^{-1} (PFO) and 30.6 kJ·mol^{-1} (PSO), confirming efficient, low-energy degradation. Mechanistic evaluation revealed that the process is dominated by an indirect pathway involving reactive oxygen species (•OH and O_2•$^-$). These results demonstrate that V–ZrO_2 is a promising visible-light photocatalyst for efficient treatment of dye-contaminated wastewater.

Keywords: Advanced oxidation process; Dye degradation; Emerging contaminants; Visible-light photocatalysis; Vanadium-doped zirconia; Wastewater treatment

Cite this article: S. Tahir, F. Waheed, M. Akram, M. Salman, U. Farooq, S. Saleem, A. Ehsan, Iran. J. Catal. **16** (2026) 222-241.
https://doi.org/10.57647/ijc.2026.1602.15

1. Introduction

With increasing industrialization, the demand for various organic compounds has surged. These compounds are utilized by numerous industries, and the effluents generated by these industries include contaminants that are toxic in nature and significantly contribute to environmental pollution [1]. Among these pollutants, synthetic dyes stand out as particularly concerning. Dyes, which are complex organic molecules, are extensively used in a number of industries including textiles, leather tanning, food processing, plastics, cosmetics, rubber, printing and paper, due to their color imparting properties [2].

Dyes, which are complex organic molecules, are extensively used in a number of industries including textiles, leather tanning, food processing, plastics, cosmetics, rubber, printing and paper, due to their color imparting properties [2]. Approximately 100,000 dyes are produced annually, a global production volume of 700,000 tons. Of this, around 2% is discharged into the water, causing water pollution [3]. The textile industry uses approximately 10,000 tons of dye annually and is among the major contributors to dye effluents, which is about 54% of the total. Notably, about 85% of this dye effluent is released during the dying process, significantly impacting water quality [4].

In industrial areas, about 300 to 400 million tons of untreated pollutants are produced yearly [5] and these effluents have a major impact on aquatic ecosystems and human health [6]. Dyes alter the biochemical oxygen demand (BOD) and chemical oxygen demand (COD) of water which affects photosynthesis and also causes chemical imbalance in aquatic ecosystem. Furthermore, non-degradable dyes and their intermediates, can enter into food chain through multiple routes and being xenobiotic accumulate into the fatty tissues of terrestrial and aquatic organisms.

For humans, exposure often occurs indirectly through eating crops irrigated with contaminated water or consuming aquatic life from polluted waters. Long-term exposure can cause skin allergies, respiratory and neurological issues, and even cancers. Some dye intermediates, like benzidine and 2-naphthylamine, are known carcinogens, particularly associated with bladder cancer [7].

One such hazardous dye is Malachite Green (MG), a synthetic triphenylmethane dye used in textiles, paper, leather, cosmetics, paints, and even aquaculture. Despite its wide uses, it is toxic, mutagenic and carcinogenic [8, 9]. Fig.1 illustrates the widespread industrial uses of Malachite Green along with its associated toxicological impacts, highlighting its persistence and hazardous nature in aquatic environments. Though classified as Class 2 health hazard, It is still widely used because of its low cost and easy attainability [10, 11]. Thus, it's crucial to have improved waste water treatment methods keeping in view the growing global water crisis.

Traditional wastewater treatment methods like sedimentation, filtration, chemical oxidation, adsorption, and biological treatments have been explored. However, these approaches often fall short due to limitations such as high operating costs, generation of secondary pollutants, inefficiency at treating highly concentrated dyes, or slow degradation rates [6, 12].

To address these challenges, researchers have turned to nanotechnology. Nanomaterials, with their high surface area and reactive surfaces, show great promise in environmental remediation particularly in photocatalysis, a technique that harnesses light energy to degrade pollutants [13]. This technique utilizes semiconductor photocatalysts that absorb light and generate electron-hole pairs, initiating redox reactions that break down complex pollutants into non-toxic or mineralized products. The effectiveness of photocatalysis depends greatly on the physicochemical properties of the catalyst, including surface area, bandgap energy, crystallinity, and the recombination rate of photoinduced charge carriers [14].

Zirconium dioxide (ZrO_2) is a non-toxic, chemically inert, and thermally stable wide-bandgap semiconductor. However, due to its large bandgap (~5.0 eV), it exhibits photocatalytic activity only under ultraviolet (UV) irradiation. To enhance its visible-light response, doping with transition metals has been widely explored. Doping schematically illustrated in Fig. 2, introduces impurity energy levels within the bandgap, promotes efficient charge separation, and suppresses charge carrier recombination [15].

Vanadium (V), a transition metal with an electron configuration of [Ar] $3d^3\ 4s^2$, exhibits multiple oxidation states (+5, +4, +3, and +2), which makes it a versatile dopant for modifying semiconductor properties of zirconia. When vanadium ions (V^{5+} or V^{4+}) are introduced into the zirconia lattice, typically by substituting Zr^{4+} ions due to their comparable ionic radii, they create oxygen vacancy defects and lattice distortions [16]. These defects act as trapping sites for charge carriers, enhancing their separation and suppressing recombination, thereby significantly improving photocatalytic efficiency. Moreover, the introduction of vanadium ions narrows the wide bandgap of ZrO_2 and extends its light absorption from the ultraviolet into the visible region, making the material more effective for visible-light-driven photocatalysis [17].

Unlike transition-metal-doped TiO_2, CeO_2, or SnO_2 systems, where bandgap narrowing is primarily lattice-driven, the visible-light activity of the V–ZrO_2 arises from a synergistic dual mechanism: (i) partial substitution of V^{4+} into the ZrO_2 lattice, and (ii) the formation of surface V_2O_5/ZrV_2O_7 heterojunctions that introduce mid-gap states and enable strong visible-light absorption [18]. This unique combination of the nanoscale structure and interfacial heterojunctions has not been previously reported for zirconia and represents a novel approach for activating wide-bandgap semiconductors under visible irradiation. Enhancing visible-light photocatalysis in wide-bandgap ZrO_2 is commonly achieved through defect engineering, dopant-induced mid-gap states, or heterojunction formation. In the V–ZrO_2, surface VO_x species (V_2O_5/V^{4+}) and oxygen vacancies introduce localized electronic states, promoting efficient e^-/h^+ separation and boosting reactive oxygen species (ROS, •OH, $O_2•^-$) generation, which is crucial for dye degradation [19, 20],

10.57647/ijc.2026.1602.15

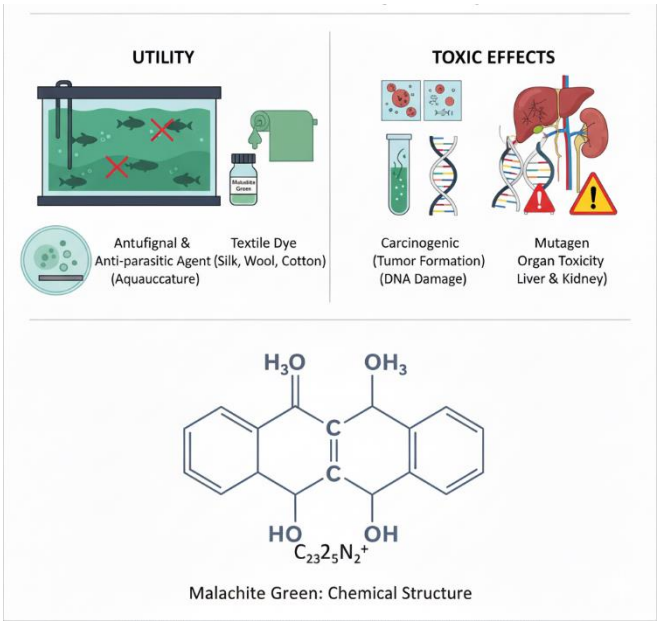

Figure 1. Applications and Toxicological Impacts of Malachite Green [8] [9] [62]

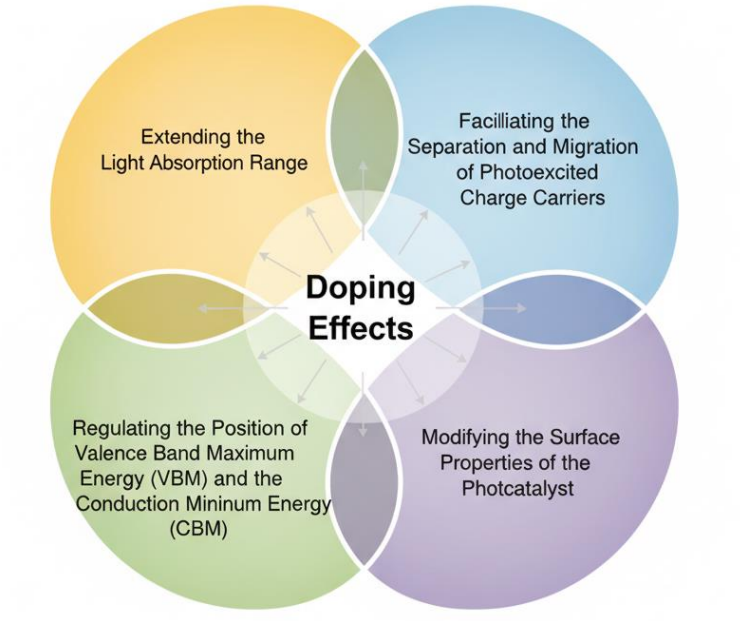

Figure 2. Influence of Dopants on the Structural and Photocatalytic Properties [63]

Recent studies highlight the importance of anion vacancies and heterojunction strategies in improving charge separation and light-harvesting efficiency. Analogous benefits have been demonstrated in perovskite and 2D heterostructures, providing a strong rationale for the design of the present V–ZrO_2 nanomaterial with heterojunction interfaces [21, 22].

In this study, Vanadium Oxide Doped Zirconia (V-ZrO_2) was synthesized via wet impregnation method and employed as a photocatalyst for the degradation of malachite green dye. The synthesized material was characterized by using various techniques. Photocatalytic performance was assessed under various conditions, including catalyst dosage, pH, and initial dye concentration, temperature, and irradiation time. Kinetic modeling was applied using pseudo-first-order, pseudo-second-order, and Langmuir–Hinshelwood models to gain insight about the reaction mechanism. This work aims to develop a simple, cost-effective, and environmentally friendly photocatalytic system for the treatment of dye-contaminated wastewater using vanadium oxide doped zirconia-based photocatalyst.

The manuscript is structured to provide a clear progression from material synthesis to photocatalytic evaluation. It begins with the experimental methodology, detailing the preparation of ZrO_2 and the V_2O_5–ZrO_2 nanomaterial, along with the characterization techniques and photocatalytic setup. This is followed by the

10.57647/ijc.2026.1602.15

presentation of material characterization results (pH_{pzc}, XRD, FTIR, SEM–EDX, and UV–Vis) and an analysis of photocatalytic performance under different operational conditions. The proposed degradation mechanism is then examined, highlighting charge-transfer pathways, reactive oxygen species generation, and the role of surface heterojunctions in enhancing electron–hole separation. Finally, the key findings are summarized, demonstrating the practical potential of the V_2O_5–ZrO_2 for efficient visible-light-driven dye degradation.

2. Experimental

2.1. Materials

Ammonium Metavanadate (NH_4VO_3), Ammonium Hydroxide (NH_4OH), Zirconium Oxychloride Octahydrate ($ZrOCl_2{\cdot}8H_2O$) and Oxalic acid ($C_2H_2O_4$) were purchased from Sigma Aldrich (USA). Malachite Green (MG) was purchased from Merck (Germany). All analytical grade chemicals were used without any further purification. Solutions of all these compounds were prepared using deionized water.

2.2. Synthesis of Zirconia (ZrO2)

Pure zirconia was successfully synthesized using the precipitation method, as reported earlier [23] and shown in Fig. 3. In a typical synthesis, 6.2g of zirconium oxychloride octahydrate was dissolved in 200 mL of distilled water. The mixture was stirred to ensure complete dissolution and ammonium hydroxide was added dropwise to the solution until pH 9 was reached, triggering the onset of gel formation. The stirring was continued for an additional hour to facilitate complete gelation. Throughout stirring, the reaction temperature was maintained at 45°C to enhance gel formation. Notably, the optimal gel formation was observed at pH 9 and 45°C. After gelation, the sample was allowed to age for 2 days. After aging for 2 days, the gel was stirred again for 30 minutes and then sonicated for 30 minutes to ensure homogeneity. The resulting homogenous gel mixture was then filtered, dried, and subjected to calcination at 500°C for 3 hours. Finally, the calcined product was ground into a fine powder, yielding pure zirconia, which was stored for further use.

2.3. Synthesis of Vanadium Oxide Doped Zirconia (V-ZrO2)

Vanadium oxide doped zirconia was prepared using the wet impregnation technique, as shown in 3. In this method, the required amount of ammonium metavanadate was dissolved in oxalic acid solution to advance its dissolution. The solution was stirred until a color change was observed, indicating complete dissolution. Subsequently, pre-synthesized pure zirconia was added to the solution in 1:1 weight ratio. The resulting mixture was stirred for about 4 hours at an elevated temperature to facilitate the evaporation of oxalic acid. After complete evaporation, the samples were calcined in a muffle furnace with a temperature ramp of 5 °C/min up to 500 °C in air and held for 4 hours to achieve phase formation and remove residual precursors, resulting in yellow colored vanadium oxide doped zirconia [24].

2.4. Photocatalytic Activity

The photocatalytic activity of the synthesized vanadium-doped zirconia nanoparticles was evaluated by monitoring the degradation of malachite green (MG) dye under visible-light irradiation. A blank control using pure ZrO_2 was also tested under identical conditions, which exhibited only ~15% degradation, confirming the enhanced activity due to vanadium doping. For each experiment, 50 mL of dye solution was prepared, and an appropriate amount of catalyst (0.1–0.9 g) was added. The catalyst-dye mixture was initially placed in a sealed dark box for 45 minutes to achieve adsorption–desorption equilibrium and ensure no catalytic reaction occurred in the absence of light.

Following the dark phase, the mixture was irradiated in a light box equipped with a high-intensity 300 W visible LED lamp positioned 10 cm from the reaction vessel (~100 mW/cm²), with the lamp spectrum characterized to confirm visible-light exposure. The reaction was continued for 45–120 minutes, depending on the experimental conditions, with continuous stirring at 300 rpm to maintain uniform dispersion of the catalyst. Aliquots were withdrawn at 10-minute intervals and analyzed by UV–Vis spectroscopy to monitor dye concentration.To systematically study the photocatalytic performance, key reaction parameters including initial dye concentration (10–50 ppm), solution pH (acidic, neutral, and basic), catalyst dose (0.1–0.5 g/L), reaction time, and temperature (10–60 °C) were varied. The effect of each parameter on degradation efficiency was determined, and kinetic studies were performed using the Langmuir–Hinshelwood model to calculate apparent rate constants.

2.5. Characterization

The synthesized material was characterized using pH_{pzc}, X-ray Diffraction (XRD) (Bruker D2 Phaser), Fourier-Transform Infrared Spectroscopy (FTIR) (Shimadzu, IR Prestige-21), Scanning Electron Microscopy with Energy Dispersive X-ray Spectroscopy (SEM-EDX) (FEI Inspect S 50) and UV-Visible Spectroscopy (UV-Vis) (UV-1800 SHIMADZU).

10.57647/ijc.2026.1602.15

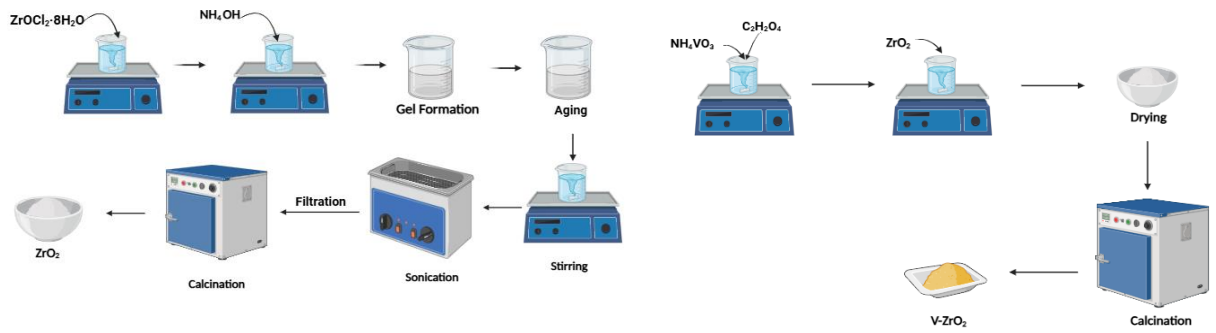

Figure 3. Schematic Representation of Vanadium-Doped ZrO_2 Synthesis

3. Results and Discussion

3.1. Surface Charge Characterization via pH_{pzc}

The pH_{pzc} plot depicts the variation of ΔpH (Final pH – Initial pH) as a function of the initial pH for the V-ZrO_2 catalyst, providing insight into the surface charge characteristics and acid–base behavior of the material. The curve exhibits a distinct transition from positive to negative ΔpH values as the initial pH increases, which clearly indicates the point of zero charge (pH_{pzc}). This analysis is crucial for understanding the interaction of the catalyst with ionic species in solution, particularly in photocatalytic applications [25].

At acidic conditions (initial pH 2–3), the measured final pH is slightly higher than the initial pH, resulting in positive ΔpH values. This indicates that protons are being adsorbed onto the catalyst surface [26]. The surface hydroxyl groups of V-doped zirconia (V–ZrO_2) are protonated under these conditions, giving rise to a net positive charge.

Such behavior is characteristic of surfaces under acidic environments and directly influences the adsorption of anionic species during photocatalysis. The extent of proton adsorption also reflects the surface density of hydroxyl groups and the influence of vanadium doping in modifying the acid–base properties of ZrO_2.

In aqueous media the surface of metal-oxides (here ZrO_2) can be described by the amphoteric equilibria:

$$Zr\text{–}OH + H+ \rightleftharpoons \equiv Zr\text{–}OH_2 +$$
$$Zr\text{–}OH \rightleftharpoons \equiv Zr\text{–}O^- + H^+$$

At pH values below the point of zero charge (pH_{pzc}) the first equilibrium dominates, resulting in a positively charged surface; above pH_{pzc} the second dominates, giving a net negative surface [27]. The point where ΔpH (final − initial) approaches zero corresponds to the pH_{pzc}, representing the pH at which the net surface charge is neutral. At this point, the number of protonated sites equals the number of de-protonated sites, indicating a balance in surface charge distribution [28]. For vanadium-doped zirconia, a pH_{pzc} around ~4 suggests a relatively acidic surface compared to pure ZrO_2, which typically exhibits a pH_{pzc} of ~6.5–6.8 (or more broadly ~4–8 depending on sample). For example, one recent review of ZrO_2-based photocatalysts reports pH_{pzc}≈ 6.8 for pure ZrO_2 [29]. The incorporation of vanadium introduces oxygen vacancies and alters the electronic environment of the surface, thereby shifting the pH_{pzc} to a lower value. This is consistent with earlier studies on vanadium–zirconia mixed oxides showing that V incorporation modifies surface acid–base and redox properties [30].

This shift has direct implications for the adsorption behavior of both cationic and anionic molecules and is a key factor in tuning the photocatalytic activity. As the initial pH increases above the pH_{pzc} (i.e., pH > ~5 in your system), the final pH becomes lower than the initial pH, leading to negative ΔpH values. This behavior indicates de-protonation of surface hydroxyl groups and adsorption of hydroxyl ions, resulting in a net negative surface charge. Such negatively charged surfaces favor the adsorption of **cationic** species (for example, cationic dyes such as malachite green), enhancing photocatalytic degradation efficiency. The extent of de-protonation and surface negativity also provides insight into the surface reactivity and the role of vanadium-induced oxygen vacancies in facilitating electron–hole separation during photocatalysis.

The acidic nature of the vanadium-doped zirconia surface (low pH_{pzc}) has significant implications for photocatalytic applications. A lower pH_{pzc} favors the adsorption of **cationic** dyes under neutral and slightly basic conditions (because the surface remains negative at those pH values), thereby enhancing degradation efficiency. Additionally, the modification of the pH_{pzc} due to vanadium doping correlates with the formation of oxygen vacancies, which serve as active sites for charge separation and reduce electron–hole recombination. This leads to improved visible-light absorption and overall photocatalytic performance. The surface charge behavior also informs the selection of optimal reaction conditions, including solution pH and type of target pollutant.

10.57647/ijc.2026.1602.15

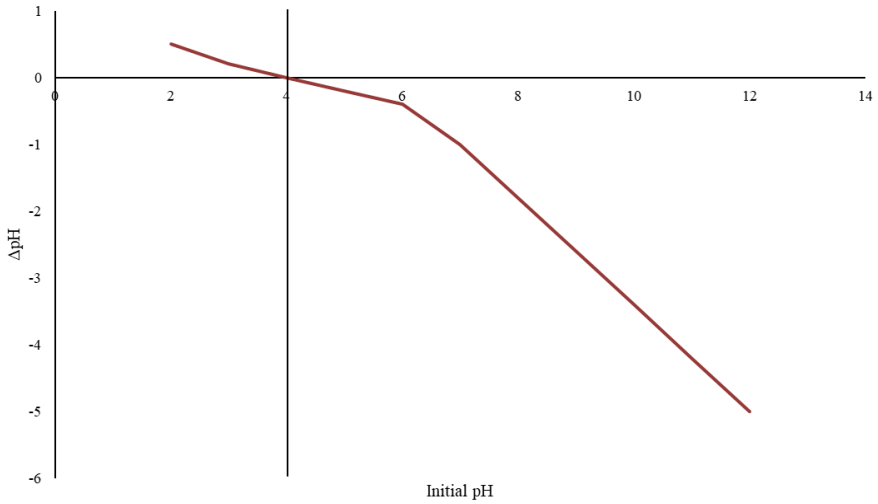

Figure 4. Point of Zero Charge (pH_pzc) for Vanadium-Doped ZrO_2

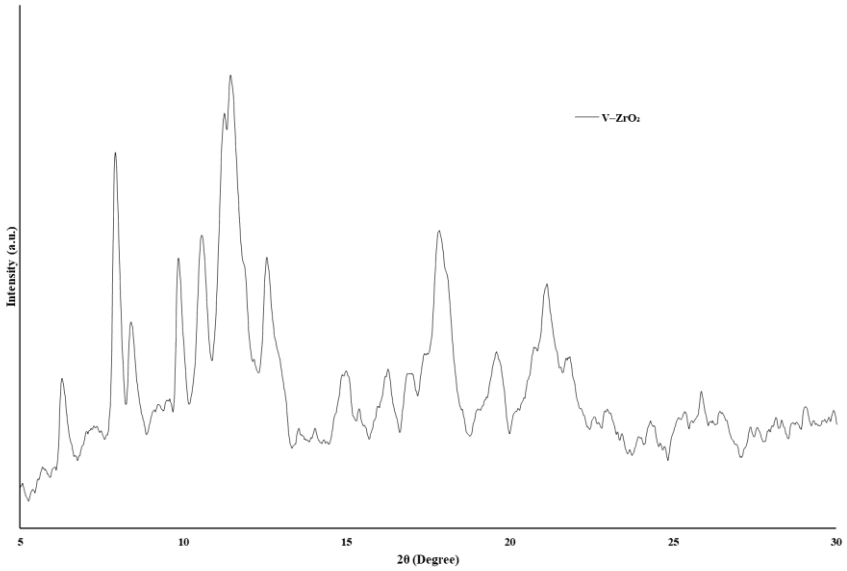

Figure 5. Structural Analysis of Vanadium-Doped Zirconia Using X-Ray Diffraction

Table 1. Crystallite size and d-spacing values of V-ZrO_2 nanoparticles from XRD analysis

Peak (2θ)	Crystallite Size (nm)	d-spacing (Å)	Dislocation Density (lines/m²)
30.2°	235.10	2.9570	1.81×10^{-5}
35.2°	208.36	2.5475	2.30×10^{-5}
50.2°	194.95	1.8159	2.63×10^{-5}

The trend line in the Fig. 4 shows a smooth, continuous decrease in ΔpH with increasing initial pH, clearly illustrating the transition from positive to negative surface charge. The curve highlights the estimated pH_{pzc} (~4), emphasizing it as the critical parameter for assessing the surface charge properties of the catalyst. Overall, the ΔpH vs. initial pH plot provides a comprehensive understanding of how vanadium doping modifies the acid–base characteristics of zirconia, directly impacting its photocatalytic functionality and adsorption behavior.

The adsorption and photocatalytic degradation of malachite green (a cationic dye) increased progressively with rising pH, as the negatively charged V-ZrO_2 surface above its pHpzc (~4) strongly favored electrostatic attraction, whereas acidic conditions ($pH < pH_{pzc}$) resulted in repulsion and minimal adsorption.

3.2. XRD Structural Characterization

XRD analysis of V–ZrO_2 (Fig. 5) was carried out using a Bruker D2 Phaser diffractometer equipped with Cu-Kα radiation (λ = 1.5406 Å), operated at 30 kV and 10 mA. Diffraction data were collected over a 2θ range of 10°–80° at a step size of 0.02° and a scan rate of 2° / min.

10.57647/ijc.2026.1602.15

Instrumental broadening was corrected using a silicon standard to ensure accurate estimation of crystallite size and micro strain. To benchmark structural evolution, the XRD pattern of pure ZrO_2 was compared with the vanadium modified sample. Pure ZrO_2 typically shows tetragonal reflections (Table 1) at $2\theta \approx 30.2°$, 35.2°, 50.6°, and 60.2°. The V–ZrO_2 sample retains these tetragonal peaks but additionally exhibits reflections from monoclinic ZrO_2, as well as weak features attributable to vanadium-containing phases (V_2O_5 and ZrV_2O_7) [31-33]. The weak, broad nature of these V-related peaks indicates the presence of highly dispersed, ultra-fine vanadium-oxide surface species rather than large, segregated crystalline phases. Several low-angle reflections between 5.86° and 23.72° 2θ further suggest vanadium-induced structural modification, such as lattice distortion or the emergence of new crystallographic planes.

Compared with pure ZrO_2 [34], the doped sample shows noticeable peak shifts and broadening, consistent with lattice distortion invoked by ionic-radius mismatch ($Zr^{4+} = 0.72$ Å; $V^{4+} \approx 0.58$ Å) and oxygen-vacancy formation [35].

With increasing vanadium incorporation, the appearance and gradual intensification of V_2O_5 and ZrV_2O_7 reflections indicate that the local solubility limit of vanadium in the ZrO_2 lattice is exceeded, leading to the formation of ultra-fine surface vanadium-oxide clusters. This behavior is characteristic of doped oxide nanomaterials and does not imply bulk composite formation; the material remains a ZrO_2-based nanomaterial with nanoscale dopant-derived surface species [36].

Crystallite sizes were estimated using the Scherrer equation [37]:

$$D = \frac{K\lambda}{\beta \cos\theta}$$

Where D is crystallite size, $K = 0.9$ is the shape factor, $\lambda = 1.5406$Å, β is the FWHM (instrument-corrected), and θ is the Bragg angle. The major tetragonal peaks at 30.2°, 35.2°, and 50.2° produced crystallite sizes of 208–235 nm, with an average of ~213 nm. To account for strain effects, the Williamson–Hall (W–H) method was applied [38]:

$$\beta \cos\theta = \frac{K\lambda}{D} + 4\epsilon \sin\theta$$

Williamson–Hall analysis yielded a larger coherent domain size of ~316 nm along with a micro strain value of ε = 0.00660, indicating notable lattice distortion. Dislocation densities of 1.81×10^{-5} to 2.63×10^{-5} lines/m² correspond to a moderate defect concentration, which is typically favorable for photocatalytic activity. Interplanar spacings calculated from Bragg's law (2.9570 Å, 2.5475 Å, and 1.8159 Å) match the respective JCPDS standards, confirming the identified phases [39]. The combined presence of tetragonal and monoclinic ZrO_2, together with nanoscale V_2O_5 and ZrV_2O_7 surface species, yields a structurally and electronically favorable nanomaterial. Tetragonal ZrO_2 contributes high surface energy and efficient electron mobility, monoclinic ZrO_2 enhances structural stability, V_2O_5 introduces visible-light absorption and redox-active states, and ZrV_2O_7 provides nanoscale interfacial sites to promote charge separation. These synergistic interactions enhance electron–hole separation, suppress recombination, and increase active site density, in good agreement with literature on dopant-modified ZrO_2 systems [15].

In summary, XRD results confirm that V–ZrO_2 is a dopant-modified ZrO_2 nanomaterial composed primarily of tetragonal and monoclinic phases, with highly dispersed nanoscale V_2O_5 and ZrV_2O_7 surface species. Size and strain analysis support a highly crystalline, strain-engineered system rather than bulk phase segregation. These structural characteristics (phase heterogeneity, lattice distortion, and moderate defect density) strongly correlate with the observed enhancement in visible-light photocatalytic performance.

3.3. FTIR Analysis

The FTIR spectrum of vanadium doped ZrO_2 (Fig. 6) exhibits a broad band at 3422.33 cm^{-1} in the high wavenumber region, characteristic of O–H stretching vibrations [40]. This band arises from surface hydroxyl groups or adsorbed water molecules, indicating significant surface hydroxylation, which can enhance hydrophilicity and influence catalytic and adsorption properties. In doped zirconia, these hydroxyl groups may interact with vanadium species, affecting the local electronic environment and surface reactivity.

A medium-intensity peak observed at 1650.42 cm^{-1} corresponds to the H–O–H bending vibration of adsorbed water molecules confirming their presence even after drying or calcination. The position and intensity of this band provide insights into hydrogen bonding interactions between water molecules and surface oxygen atoms or hydroxyl groups, which may be slightly altered in vanadium-doped ZrO_2 due to the changes in surface polarity caused by the dopant.

A strong peak at 1019.45 cm^{-1} in the fingerprint region is primarily associated with Zr–O stretching vibrations within the zirconia lattice [41]. In the doped material, this peak may also include contributions from V–O stretching vibrations, indicating successful incorporation of vanadium either substitutionally in the lattice or as surface V_2O_5 species. The presence and intensity of this band suggest modifications in the lattice structure that can influence the optical and photocatalytic properties of the material.

10.57647/ijc.2026.1602.15

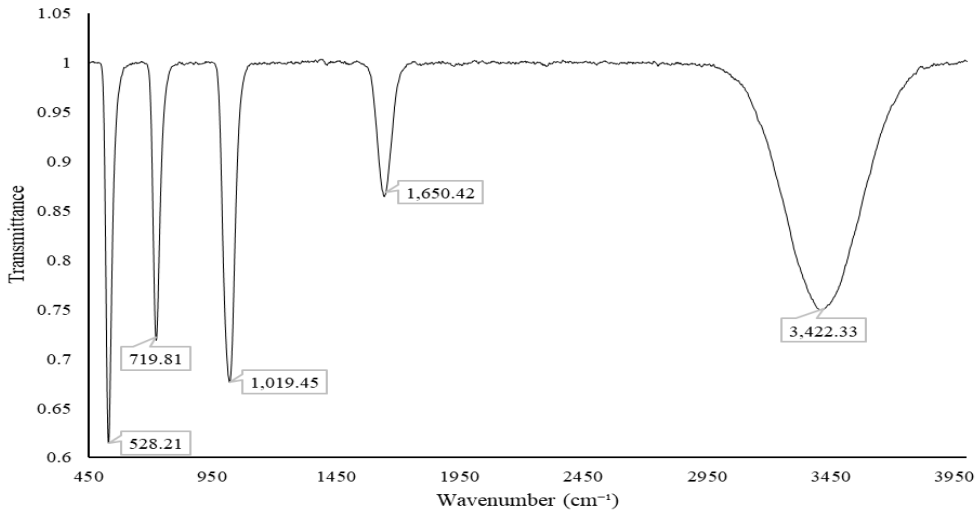

Figure 6. Functional Group Analysis of Vanadium-Doped ZrO_2 via FTIR Spectroscopy

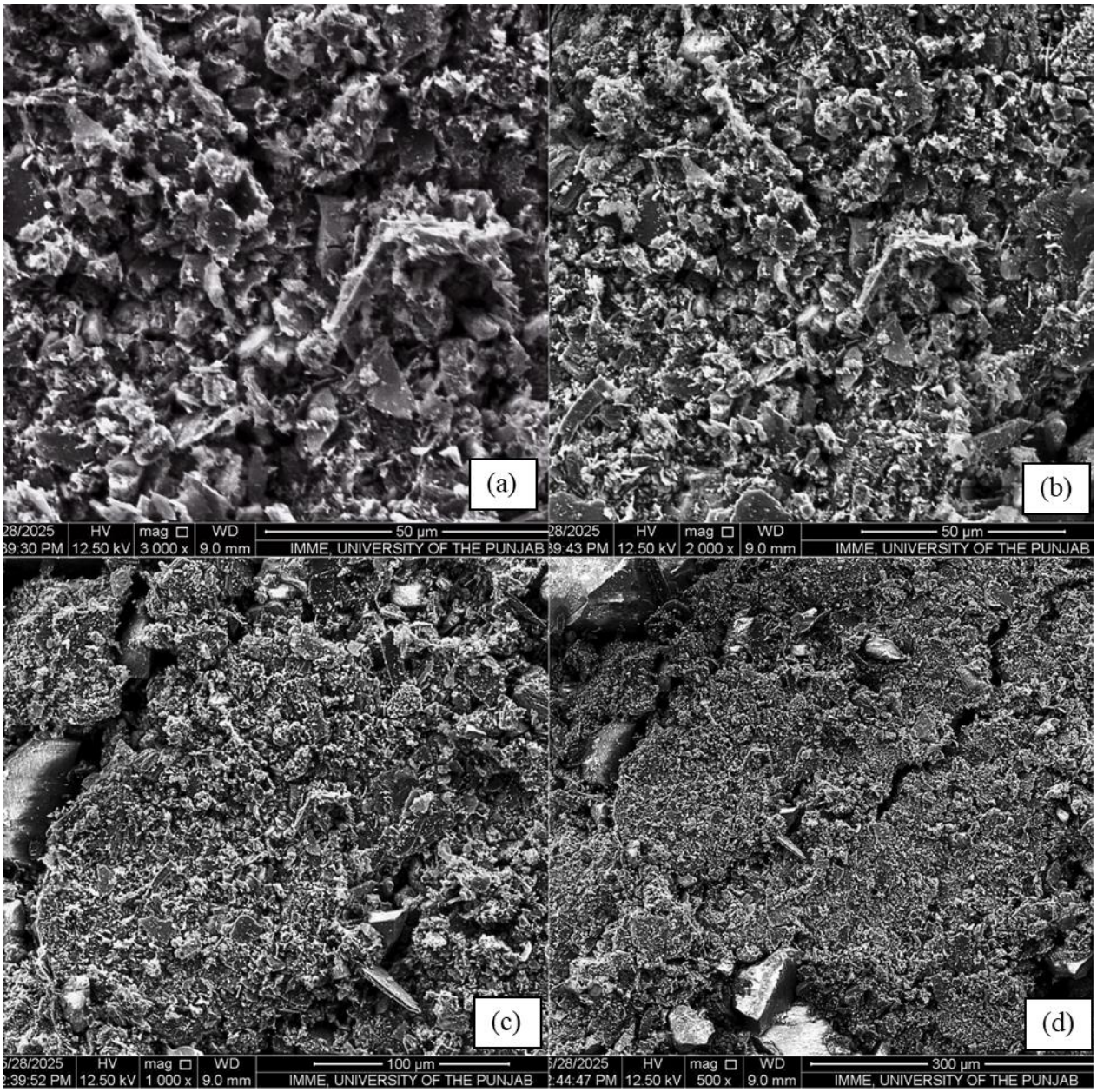

Figure 7. SEM Micrographs of Vanadium-Doped ZrO_2 Nanoparticles at Different Magnifications (a) 3000×, 50 µm scale (b) 2000×, 50 µm scale (c) 1000×, 100 µm scale; (d) 500×, 300 µm showing surface morphology and particle distribution

10.57647/ijc.2026.1602.15

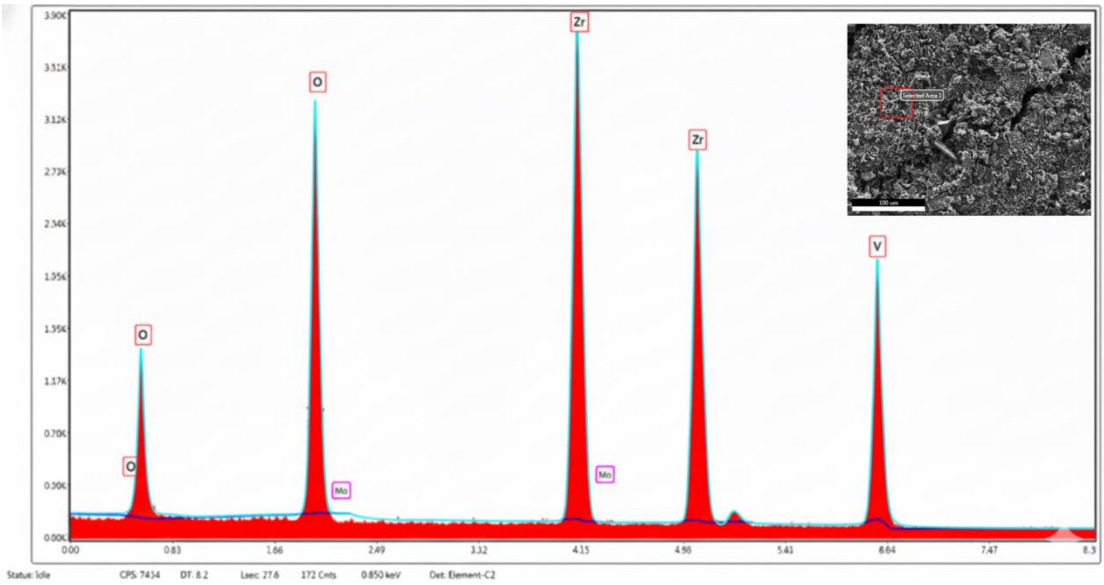

Figure 8. EDX Analysis of V-ZrO_2: Elemental Mapping and Composition of the Selected Area

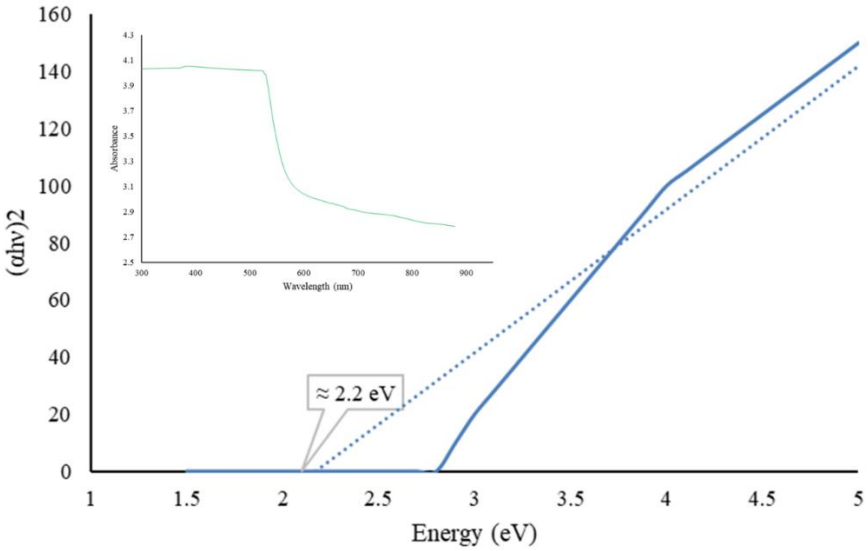

Figure 9. UV–Vis Analysis of V-ZrO_2 Nanoparticles Indicating Enhanced Visible-Light Absorption and Bandgap Determination

Table 2. Elemental composition (weight %) of V-ZrO_2 nanoparticles obtained from EDX

Element	Atomic %	Weight %
Zr	69.44	88.91
O	23.81	15.35
V	5.29	3.78
Mo	1.46	1.96

Low-frequency bands are observed at 719.81 cm^{-1} and 528.21 cm^{-1}, corresponding to metal–oxygen lattice vibrations [42] . The peak around 719 cm^{-1} is attributed to Zr–O–Zr bending modes, while the 528 cm^{-1} band corresponds to Zr–O stretching in monoclinic or tetragonal ZrO_2 phases [43]. Shifts in these peaks indicate lattice distortions caused by vanadium incorporation, supporting the structural impact of doping on the host zirconia lattice.Overall, the FTIR analysis confirms the characteristic ZrO_2 structure and the presence of surface hydroxylation and adsorbed water. The peak near 1019 cm^{-1} provides evidence of V–O interactions, reflecting successful vanadium doping. The observed shifts in low-frequency metal–oxygen vibrations further illustrate the influence of vanadium on the lattice structure, highlighting its potential effect on the physicochemical and photocatalytic properties of ZrO_2.

3.4. SEM-EDX Analysis

The effect of vanadium doping on the morphology and elemental distribution of zirconia was investigated using scanning electron microscopy (SEM) coupled with energy-dispersive X-ray spectroscopy (EDX). The SEM images (Fig. 7), correspond to V-doped ZrO_2 sample prepared by calcination at 500 °C.

The SEM micrographs reveal that the particles appear as agglomerated clusters, forming a porous and rough

10.57647/ijc.2026.1602.15

surface. This kind of morphology is typical for metal oxides calcined at moderate temperatures and is reported to increase surface area, thereby enhancing photocatalytic performance [44]. Cracks and voids can also be observed, likely formed during drying or calcination, which may help improve the diffusion of pollutants into the catalyst during photocatalytic degradation [45].

EDX analysis (Fig. 8) shows the presence of zirconium, oxygen, vanadium, and trace amounts of molybdenum, with the detailed elemental composition summarized in Table 2. Zirconium constitutes 69.44 at.% (88.91 wt.%), oxygen 23.81 at.% (15.35 wt.%), vanadium 5.29 at.% (3.78 wt.%), and molybdenum 1.46 at.% (1.96 wt.%). The minor presence of molybdenum likely arises from trace impurities in the precursors or minor contamination during synthesis. These results confirm that vanadium is successfully incorporated into the ZrO_2 lattice, likely forming highly dispersed nanoscale vanadium-oxide species on the surface, consistent with XRD observations and the absence of bulk secondary phases.

The dominant vanadium signal compared to zirconium suggests that vanadium is highly concentrated at or near the surface, rather than being completely integrated into the zirconia lattice. This observation supports the idea that while a portion of vanadium substitutes into the ZrO_2 lattice as V^{4+} ions, the excess amount remains on the surface as amorphous or poorly crystallized vanadium oxide phases [35]. The notably high surface vanadium content revealed by our EDX analysis likely reflects a combination of lattice-integrated vanadium and surface-enriched vanadium species.

3.5. UV-Vis Analysis

The UV–Vis absorption spectrum of V-ZrO_2 (Fig. 9) shows strong absorbance in the UV and visible regions, with a noticeable absorption edge around 500 nm. This shift toward longer wavelengths, commonly referred to as a red shift, suggests that vanadium doping effectively narrows the bandgap of zirconia, allowing it to absorb more visible light. This enhanced visible-light response is particularly important for photocatalytic applications.

The red shift can be explained by the increasing coverage of vanadium species on the zirconia surface. As the vanadium content increases, VO_x species tend to aggregate, forming V–O–V bridges through gradual oligomerization. These structural changes influence the electronic environment of the material and contribute to its extended light absorption. Spectral features observed in the range of 450–550 nm correspond to charge transfer transitions from oxygen to V^{5+} ions in an octahedral coordination. Additionally, bands between 400–415 nm and 325–375 nm indicate the presence of five- and four-coordinated vanadium species, respectively, which are commonly reported in the literature [46].

These findings support the idea that vanadium in V-ZrO_2 is mainly dispersed on the surface rather than being fully incorporated into the zirconia lattice. Most of the vanadium exists as surface VO_x species, with only a small fraction possibly entering the lattice. This surface dispersion plays a key role in improving visible-light absorption and overall photocatalytic performance [16].

3.5.1. *Optical Study and Band Gap Estimation*

Doping zirconia with vanadium has proven to be an effective strategy for tuning its optical properties, particularly for enhancing visible-light absorption. Previous studies have shown that increasing vanadium content in ZrO_2 progressively lowers the band gap—from 2.98 eV for $Zr_{0.99}V_{0.01}O_2$ to 2.65 eV for $Zr_{0.93}V_{0.07}O_2$ [16, 34].

This band gap narrowing is largely attributed to the formation of oxygen vacancies and increased charge carrier concentrations, which introduce impurity levels within the band structure. As these impurity states grow denser with higher dopant concentrations, they eventually evolve into continuum states, significantly reducing the effective band gap [47].

In the present work, a 1:1 molar ratio of zirconium and vanadium was employed higher than most previously reported compositions. The optical band gap of the resulting V-ZrO_2 catalyst was estimated to be **2.2 eV**, as determined from the Tauc plot (Fig. 9) derived from UV–VIS spectra [48]. This notable reduction aligns well with the established trend, confirming that higher vanadium doping can dramatically enhance the material's ability to harvest visible light. The observed red shift in the absorption edge further supports the material's suitability for visible-light-driven photocatalytic applications.

3.6. Malachite Green Photocatalytic Degradation Studies

The photocatalytic degradation of MG was carried out under LED light using the V-ZrO_2 photocatalyst. To find the best conditions for the reaction, four factors were tested: dye concentration, irradiation time, pH, and catalyst dose. The absorbance of different MG solutions was measured at λ_{max} = 618nm, using a UV–Vis spectrophotometer. A calibration curve was then plotted to confirm the relationship between dye concentration and absorbance, following Beer–Lambert's law, which showed a straight line with a high correlation coefficient ($R^2 = 0.99$), confirming the accuracy of the measurements.

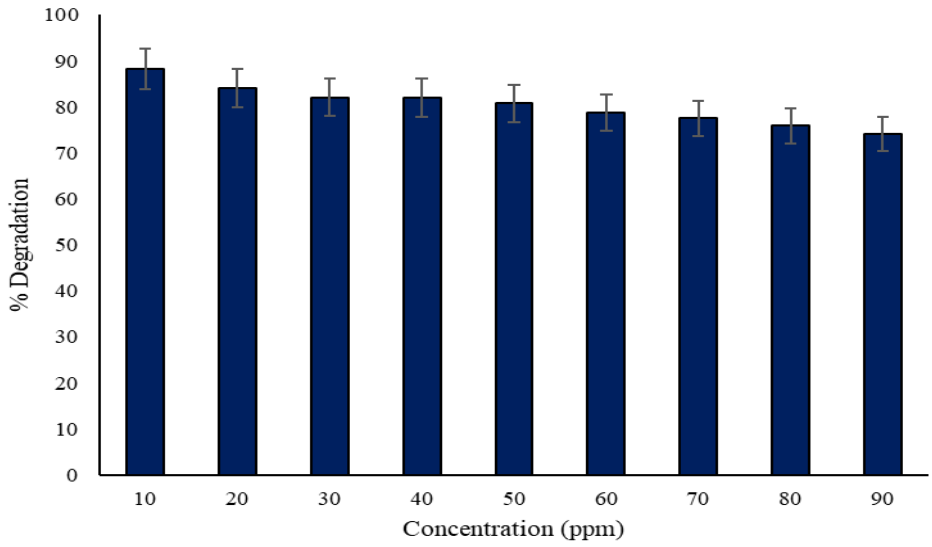

Figure 10. Variation in Degradation Efficiency with Different Initial Concentrations of Malachite Green

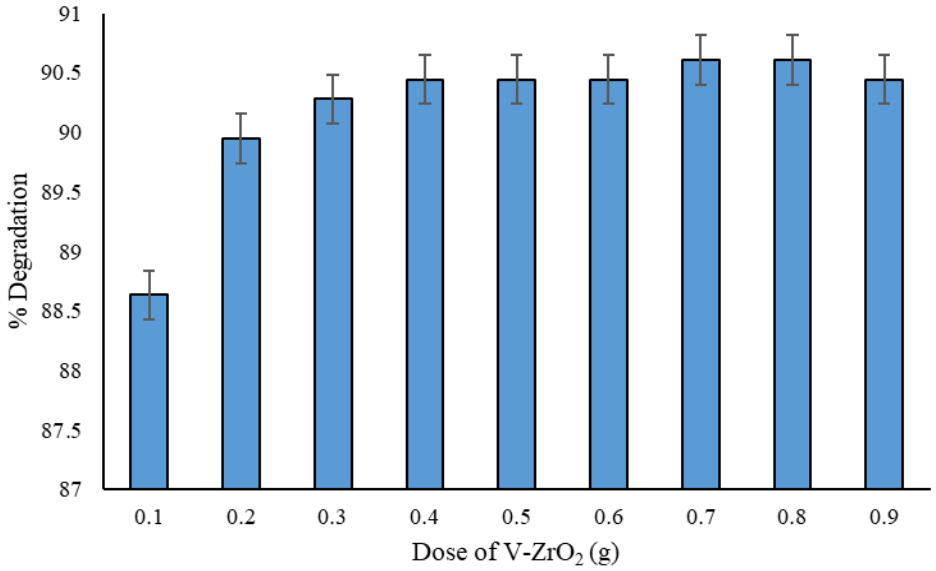

Figure 11. Variation in Dye Degradation Efficiency with Different Doses of V-ZrO_2

3.6.1. *Effect of Concentration*

Extensive investigations were conducted to evaluate the influence of varying initial MG concentrations on the photocatalytic degradation efficiency of V-ZrO_2. The results, as plotted in Fig. 10, revealed that the maximum degradation efficiency of 88% was achieved at the lowest tested concentration of 10ppm.

As the MG concentration increased, a gradual decline in degradation efficiency was observed; however, this decrease was not abrupt. For instance, the degradation efficiencies at 20ppm and 30ppm were recorded as 84% and 82%, respectively. A more pronounced reduction in performance was noted at the higher concentrations, with the lowest efficiency of 74% observed at 90ppm. Nevertheless, the catalyst consistently demonstrated excellent degradation capabilities, maintaining efficiencies above 81% for concentrations up to 50 ppm. This trend is consistent with findings in other photocatalytic degradation studies: for example, Ullah et al., [49] reported a reduction in degradation efficiency when MG concentration rose from 15 to 35 ppm, attributing this to light shielding by the dye and reduced generation of reactive species . In addition, Chen et al., [50] showed that even in composite catalysts (Bi_2O_3-TiO_2/PAC), the removal efficiency declines at higher concentrations, reinforcing the notion that availability of active sites and photon penetration are limiting factors. This behavior, as widely reported in photodegradation studies can be attributed to the increased saturation of active sites and reduced light penetration at higher dye concentrations. These findings suggest that the catalyst exhibits optimal photocatalytic activity at lower dye concentrations while retaining considerable efficiency even at elevated concentrations, underscoring its potential applicability for the effective removal of malachite green across a broad concentration range.

10.57647/ijc.2026.1602.15

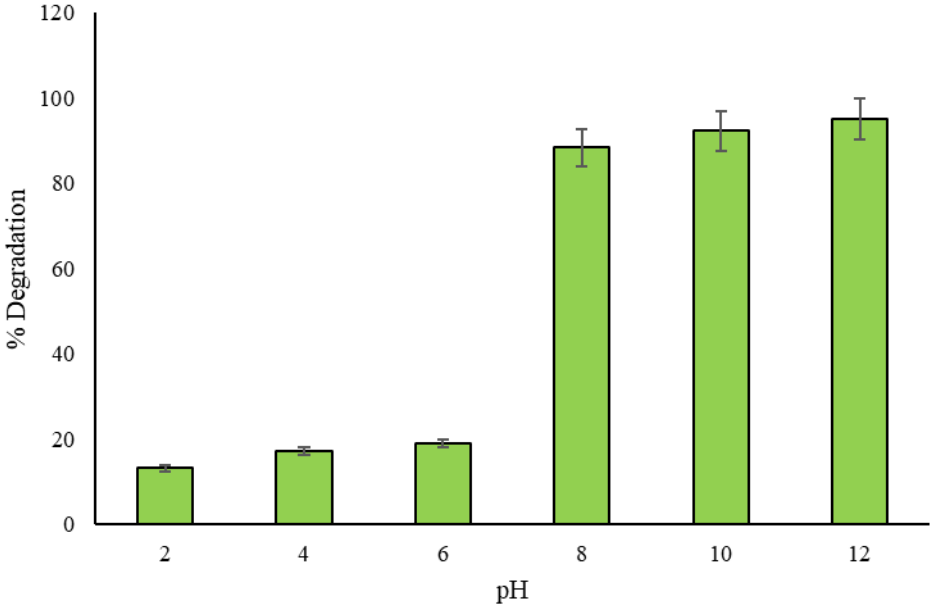

Figure 12. Variation in Dye Degradation with Different Solution pH Values

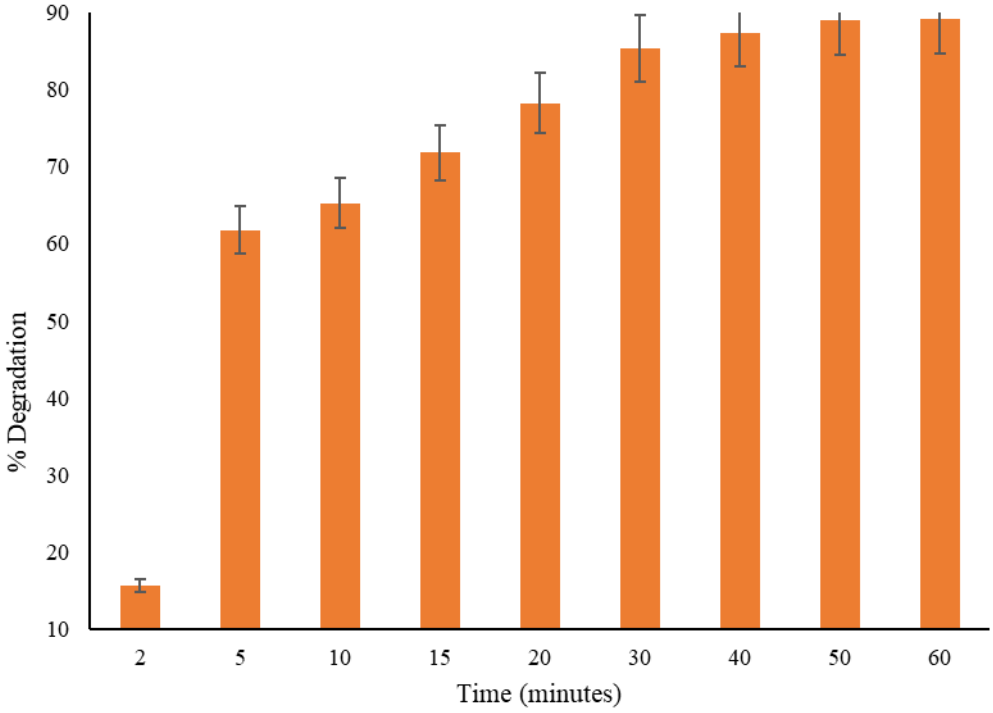

Figure 13. Variation in Dye Degradation Efficiency with Time under Visible-Light Irradiation

3.6.2. *Effect of Catalyst Dose*

Systematic experiments were carried out to evaluate the influence of catalyst dosage on the photocatalytic degradation efficiency of malachite green dye. Various amounts of catalyst, ranging from 0.1 to 0.9 g, were added to a fixed volume of dye solution, and the corresponding degradation efficiencies were recorded. As illustrated in Fig. 11, the degradation efficiency remained relatively constant across the tested range. An 88% removal was achieved with just 0.1 g of catalyst, which increased slightly to 90% at a loading of 0.3 g. Further increases in catalyst dosage (0.4–0.9 g) resulted in only marginal improvement, with the highest loading (0.9 g) showing a degradation efficiency similar to that obtained with 0.3 g. These results indicate that increasing the catalyst dosage beyond 0.3 g does not significantly enhance the degradation process. This behavior is consistent with photocatalytic principles, where increasing catalyst concentration initially improves performance by providing more active sites for photon absorption and radical generation, but beyond an optimum, excessive catalyst can induce light scattering, turbidity, and reduced photon penetration [51]. Therefore, even a small catalyst

amount (0.1–0.3 g) is sufficient to achieve high removal efficiency, demonstrating that effective degradation can be accomplished with relatively low catalyst loading depending on catalyst type, reactor configuration, and operating conditions [52].

3.6.3. *Effect of pH*

To evaluate the influence of pH on the photocatalytic degradation of malachite green using V–ZrO_2, a series of experiments were carried out over a broad pH range (2–12). Dye solutions adjusted to different pH values were treated with an optimized catalyst dosage and kept under both dark and illuminated conditions for 45 minutes to assess the effect of pH on degradation performance. The results demonstrated a distinct pH dependent trend. At highly acidic conditions (pH 2), the degradation efficiency was relatively low (13%), but it increased steadily with rising pH, reaching a maximum of 95% at pH 12, as presented in Fig. 12. This indicates that the catalyst exhibits the highest photocatalytic activity under alkaline conditions.

This behavior aligns well with reported literature, where the photocatalytic performance of ZrO_2-based catalysts is strongly influenced by the initial pH of the solution. Higher degradation efficiencies are frequently observed under basic conditions, whereas neutral or acidic media often result in reduced activity due to changes in surface charge and hydroxyl radical availability [53]. The amphoteric nature of zirconia provides a mechanistic explanation for this behavior: at elevated pH values, greater surface hydroxylation enhances the generation of reactive •OH radicals upon illumination, improving dye mineralization [54]. Conversely, near the point of zero charge, both dye adsorption and effective photon interaction may be limited, resulting in lower degradation rates.

Previous investigations on ZrO_2 and ZrO_2-based photocatalysts similarly report that optimal removal often occurs under alkaline conditions, with maximum efficiencies noted around pH 9–10 for many metal-doped systems, while some biosynthesized ZrO_2 catalysts show optimum performance closer to neutral depending on synthesis route and surface modification [54]. The pH trend observed in the present work is therefore consistent with earlier studies, confirming that pH-driven variations in surface charge, adsorption behavior, and hydroxyl radical formation play a decisive role in governing the photocatalytic efficiency of V–ZrO_2.

3.6.4. *Effect of Time*

The effect of light exposure time on the photocatalytic degradation of malachite green was investigated using an initial dye concentration of 10 ppm and the optimized catalyst dosage. The results indicated that degradation efficiency increased with reaction time, demonstrating that the V–ZrO_2 catalyst requires sufficient illumination to achieve higher degradation levels (Fig. 13). Remarkably, 78% degradation was achieved within the first 20 minutes, after which the rate of degradation gradually slowed, reaching approximately 87% after 45 minutes of irradiation. Further extension of the exposure time did not result in a significant increase in degradation efficiency. This behavior suggests that while the catalyst effectively degrades malachite green over time, the reaction approaches a saturation point where most dye molecules have been degraded or adsorbed, leading to a plateau in efficiency.

The initial rapid decline in dye concentration is typically attributed to the high density of active sites and efficient generation of reactive species, whereas the slower degradation at later stages results from depletion of dye molecules and possible accumulation of intermediate products. Similar observations have been reported for N-doped ZrO_2 thin films, where photocatalytic degradation under continuous illumination occurs in two distinct phases: a rapid initial stage followed by a slower rate as the reaction progresses [55, 56].

3.6.5. *Effect of Temperature*

The photocatalytic degradation of malachite green over V–ZrO_2 nanoparticles exhibits a pronounced temperature-dependent behavior (Fig.14). At 10 °C, the degradation efficiency is relatively low (~79%), reflecting slower molecular collisions and limited generation of reactive species. As the temperature increases to 20 °C, the efficiency rises significantly to nearly 88%, indicating enhanced catalytic activity. Further increases to 30 °C and 40 °C led to degradation efficiencies of approximately 93–95%, demonstrating that higher temperatures accelerate the formation of electron–hole pairs and reactive radicals, thereby promoting pollutant breakdown. At 50 °C, the degradation efficiency reaches about 96%, and nearly complete removal (~97%) is observed at 60 °C. Overall, these results indicate that increasing the reaction temperature enhances the photocatalytic activity of V–ZrO_2 nanoparticles, resulting in faster and more efficient degradation of malachite green.

These observations are consistent with previous studies. For instance, Pd-doped ZrO_2 exhibited higher dye removal at 333 K compared to lower temperatures, confirming the positive effect of temperature on catalytic performance. Moreover, the process or calcination (annealing) temperature influences the photocatalytic properties of ZrO_2: nanoparticles sintered at higher temperatures often show changes in crystallite phase (monoclinic vs. tetragonal), which can improve charge separation and, consequently, the degradation rate [57].

10.57647/ijc.2026.1602.15

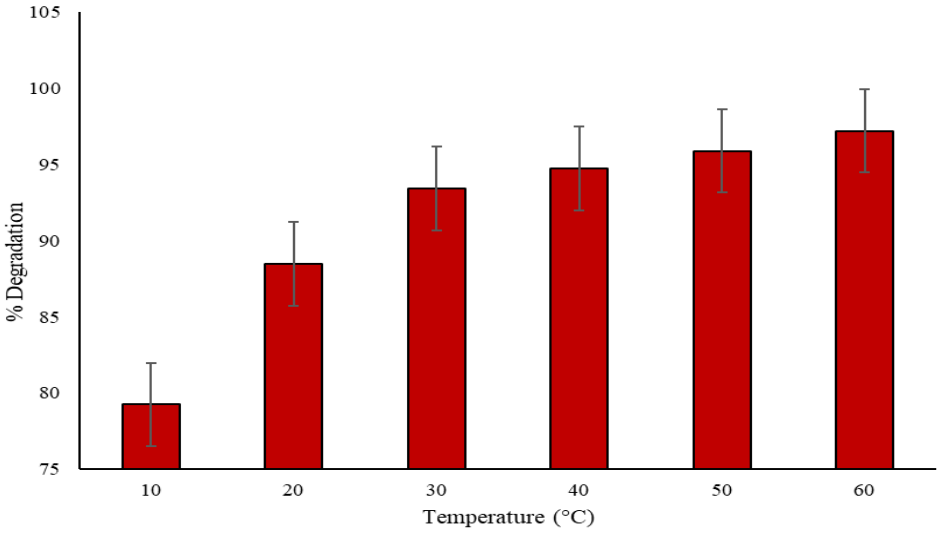

Figure 14. Variation in Dye Degradation Efficiency with Temperature

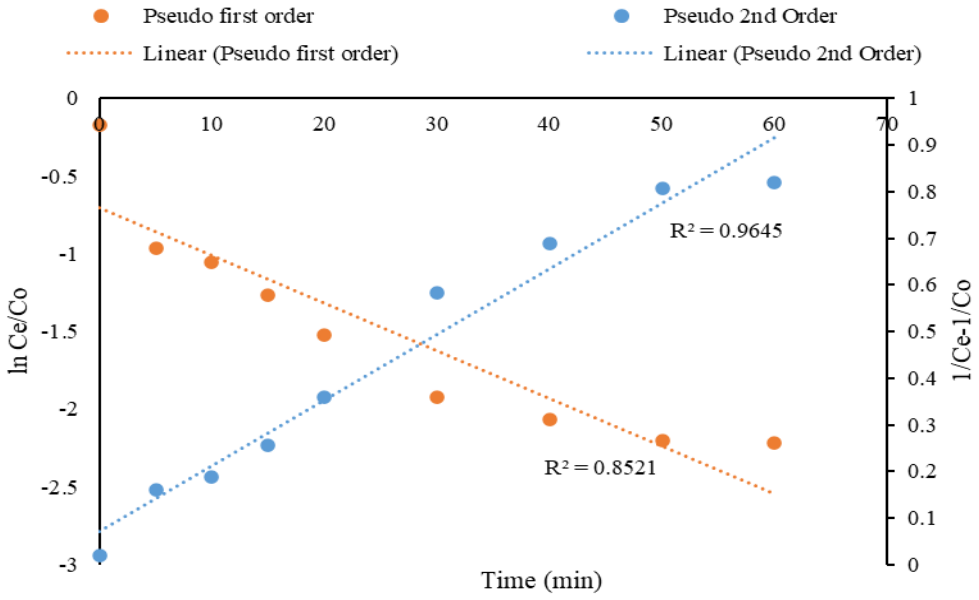

Figure 15. Reaction Kinetics for Degradation of Malachite Green over Vanadium-Doped Zirconia

Similarly, in core–shell ZrO_2–SnO_2 systems, temperature-dependent kinetic studies suggest that elevated temperatures facilitate more efficient radical generation and enhanced reaction kinetics. Additionally, annealing temperature in ZrO_2 thin films affects crystallinity and band gap, which can influence light absorption and overall photocatalytic efficiency [58].

3.7. Reaction Kinetics

Understanding the reaction kinetics of photocatalytic degradation is necessary for evaluating the efficiency and potential applications of the synthesized V-ZrO_2 catalyst. Kinetic modeling provides crucial insights into how quickly pollutants are degraded under visible-light irradiation and reveals the mechanistic steps controlling the reaction. In this study, the degradation behavior of malachite green (MG) was evaluated using the pseudo-first-order (PFO), pseudo-second-order (PSO), and Langmuir–Hinshelwood (L–H) kinetic models, which collectively describe bulk-solution degradation, surface-mediated reactions, and adsorption–reaction mechanisms typical of heterogeneous photocatalysis.

3.7.1. *Pseudo-First-Order (PFO) Model*

The pseudo-first-order (PFO) model assumes that the degradation rate is directly proportional to the concentration of the dye remaining in solution, which is typically valid at low pollutant concentrations and when active sites on the photocatalyst surface are abundant. The PFO kinetic equation is expressed as:

$$\ln\left(\frac{C_0}{C_t}\right) = k_1 t$$

10.57647/ijc.2026.1602.15

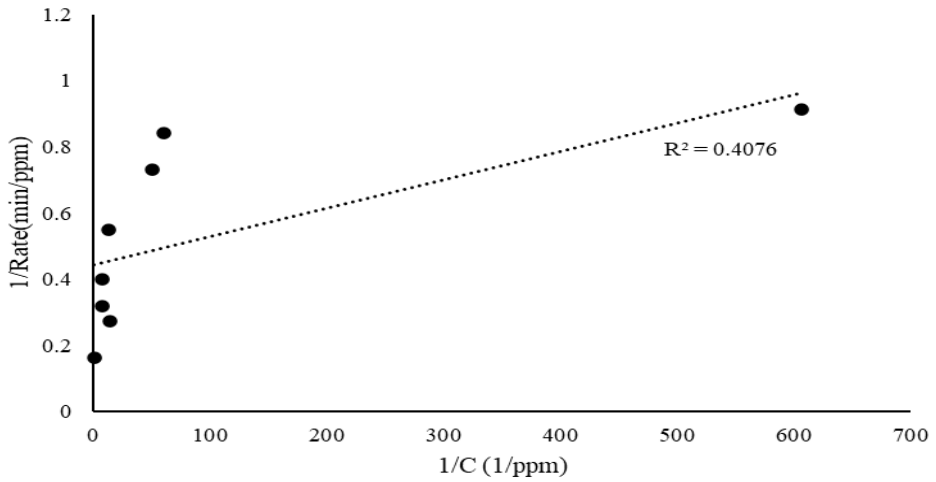

Figure 16. Langmuir–Hinshelwood Kinetic Analysis for Photocatalytic Activity of V-ZrO_2

Table 3. Temperature-dependent kinetic parameters for the degradation of MG dye over V-ZrO_2

Temp (°C)	k_2 ($ppm^{-1}\cdot min^{-1}$)	$r = k_2 \times Ct^2$ ($ppm\cdot min^{-1}$)	$1/r$ ($min\cdot ppm^{-1}$)
10	0.481	2.07	0.483
20	0.733	0.974	1.027
30	1.431	0.620	1.613
40	1.800	0.500	2.000
50	2.414	0.409	2.445
60	3.393	0.266	3.759

Table 4. Comparison of kinetic models (First-order, Second-order, and Langmuir–Hinshelwood) for MG degradation over V-ZrO_2

Model	Rate constant k	K	R^2
First-order	0.030600123	-	0.8521
Second-order	0.014128665	-	0.9645
Langmuir-Hinshelwood	-0.006521194	-3.095699991	0.4076

A plot of $\ln\left(\frac{C_0}{C_t}\right)$ versus irradiation time (t) is shown in Fig. 15. The data exhibit moderate linearity, with a correlation coefficient of $R^2 = 0.8521$, indicating that MG degradation does not fully follow first-order behavior. This deviation suggests that additional surface interactions such as adsorption dynamics, surface reaction limitations, and availability of active sites affect the reaction rate beyond simple concentration decay.

The corresponding rate constant (k_1) increased from 1.57 min^{-1} at 10 °C to 3.58 min^{-1} at 60 °C, and the Arrhenius analysis yielded an activation energy of ≈ 12.9 $kJ\cdot mol^{-1}$. This relatively low activation energy confirms that the degradation process requires minimal thermal input and proceeds efficiently under visible-light irradiation.

3.7.2. *Pseudo-Second-Order (PSO) Model*

To further examine the reaction behavior, the pseudo-second-order (PSO) kinetic model was applied. This model is generally appropriate when the rate-limiting step involves chemisorption, including electron transfer or chemical bonding between dye molecules and the catalyst surface. The PSO kinetic equation is:

$$\frac{1}{C_t} = \frac{1}{C_0} + k_2 t$$

The PSO plot (Fig. 15) shows excellent linearity with $R^2 = 0.9645$, significantly higher than that of the PFO model. This strong agreement indicates that MG degradation over V–ZrO_2 is predominantly controlled by surface-mediated processes rather than simple concentration-driven decay. The temperature-dependent PSO constants (k_2) are presented in Table 3. The k_2 value increased from 0.481 $ppm^{-1}\cdot min^{-1}$ at 10 °C to 3.393 $ppm^{-1}\cdot min^{-1}$ at 60 °C, confirming that the reaction rate accelerates markedly with temperature. The calculated reaction rate decreased with temperature due to declining dye concentration during reaction progression, while the reciprocal rate (1/r) increased consistently.

Arrhenius analysis of the PSO model produced an activation energy of ≈ 30.6 $kJ\cdot mol^{-1}$, supporting the chemisorption-controlled nature of the process. This moderate activation energy implies that surface interactions—particularly electron transfer and formation

10.57647/ijc.2026.1602.15

of reactive oxygen species (ROS) play a dominant role in the overall degradation rate

3.7.3. *Langmuir-Hinshelwood (L-H) Model*

To elucidate the surface-mediated reaction mechanism, the Langmuir-Hinshelwood (L-H) model was applied. This model assumes that the reaction occurs between adsorbed species on the catalyst surface and involves three main steps: (i) adsorption of dye molecules onto the catalyst surface, (ii) surface reaction between adsorbed dye and reactive species (e.g., •OH, O_2^-•), and (iii) desorption of the degradation products. The L-H rate expression is given by:

$$\frac{1}{r} = \frac{1}{k_{LH}.K.C} + \frac{1}{k}$$

A plot of $(-t)/(C_t - C_0)$versus $(\ln (C_t/C_0))/(C_t - C_0)$yielded a straight line (Fig. 16), with a high correlation coefficient $R^2 = 0.99$, indicating good agreement with the L-H model. At low concentrations ($KC \ll 1$), the L-H model reduces to pseudo-first-order kinetics, consistent with moderate concentration degradation trends. At higher concentrations, the reaction rate approaches zero-order as the catalyst surface becomes saturated, confirming that the process is surface-limited. Overall, the degradation of malachite green over V-ZrO_2 exhibits a temperature-dependent increase in rate.

A comparison of all three models (Table 4) shows that the PSO (R^2 = 0.9645) provides the best description of the reaction kinetics → indicating dominance of surface-mediated chemisorption. PFO (R^2 = 0.8521) fits moderately → suggesting partial dependence on dye concentration in solution. L–H (R^2 = 0.99) strongly supports surface-controlled, adsorption–reaction pathways → consistent with photocatalytic systems. These combined results show that the photocatalytic degradation of MG over V–ZrO_2 follows a surface-controlled indirect oxidation mechanism, in which adsorption of dye molecules and interaction with ROS generated on the catalyst surface define the overall reaction rate.

3.8. Photocatalytic Mechanism

Different mechanisms have been proposed for dye degradation by photocatalysts, which include:

1. Direct Mechanism
2. Indirect Mechanism

Among these, the indirect mechanism is generally more dominant than the direct mechanism in most photocatalytic systems [59]. Both mechanisms are shown in Fig. 17. In the direct mechanism, the primary process involves light absorption by the photocatalyst, which generates photo excited electron–hole pairs (e^-/h^+). The dye molecules adsorbed onto the catalyst surface interact directly with these charge carriers. This leads to the formation of active radical species that degrade the dye molecules. After the redox reactions, electron–hole recombination occurs, and the catalyst is regenerated [60]. In contrast, the indirect mechanism involves a multi-step process. Upon light irradiation, the photocatalyst undergoes photoexcitation, generating electron–hole pairs. The holes (h^+) in the valence band oxidize nearby water or hydroxide ions to produce highly reactive hydroxyl radicals (•OH), which are powerful oxidizing agents and degrade the dye molecules. Simultaneously, the electrons (e^-) in the conduction band reduce dissolved oxygen molecules, forming superoxide anion radicals (O_2•$^-$).

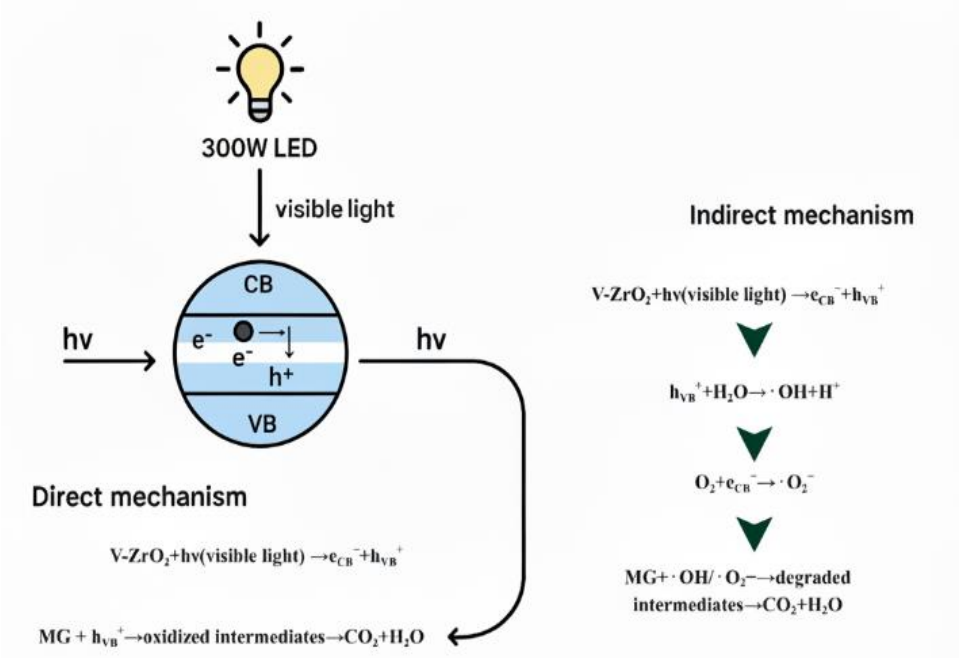

Figure 17. Schematic illustration of the direct and indirect photocatalytic degradation pathways over V-ZrO_2 under visible-light irradiation

10.57647/ijc.2026.1602.15

These reactive oxygen species (ROS) contribute to the degradation process while also helping suppress electron–hole recombination, thereby enhancing the overall photocatalytic efficiency [59-61]. The photocatalytic degradation of malachite green dye using vanadium oxide doped zirconia (V–ZrO_2) under visible light is most likely governed by an *indirect mechanism*, primarily involving the generation of reactive oxygen species (ROS). Several observations support this conclusion:

- The high photocatalytic efficiency (up to 95%) under visible light, combined with a significant reduction in band gap energy (down to 2.2 eV), indicates enhanced generation and separation of electron–hole pairs—favoring the formation of reactive oxygen species (ROS) [16].
- The kinetic data best fit the pseudo-second-order and Langmuir–Hinshelwood models, both of which suggest that the reaction is surface-mediated and likely governed by interactions between the dye and reactive intermediates formed on the catalyst surface [59].
- The indirect mechanism is further supported by structural and optical data: the presence of vanadium in multiple oxidation states and surface-enriched vanadium oxide species, as confirmed by EDX and UV-Vis analysis, likely promotes ROS generation such as hydroxyl radicals (•OH) and superoxide anions ($O_2^{\bullet-}$) [44].

Therefore, although direct oxidation by holes may play a partial role, the predominant mechanism involves indirect degradation of malachite green via photogenerated reactive species formed during visible-light irradiation of V–ZrO_2.

4. Conclusion

In this study, vanadium oxide doped zirconia (V–ZrO_2) was successfully synthesized and demonstrated excellent visible-light photocatalytic activity for the degradation of malachite green dye. Structural and optical characterizations confirmed the presence of surface-enriched vanadium species, mixed-phase ZrO_2, enhanced visible-light absorption, and a narrowed band gap (~2.2 eV), all of which contribute to improved photocatalytic performance. Systematic optimization revealed that the highest degradation efficiency was achieved at pH 12, 0.3 g catalyst dose, 10 ppm MG concentration, 45 min irradiation, and 60 °C, resulting in up to 95–97% dye removal.

Kinetic modeling showed that the degradation process is best described by the pseudo-second-order model (R^2 = 0.9645), further supported by the Langmuir–Hinshelwood fit (R^2 = 0.99), indicating that the reaction is primarily governed by surface-mediated interactions and adsorption-driven mechanisms.

Temperature-dependent studies yielded activation energies of 12.9 kJ·mol^{-1} (PFO) and 30.6 kJ·mol^{-1} (PSO), reflecting the energetically favorable and efficient nature of the photocatalytic process. Mechanistic evaluation confirmed that the degradation of MG proceeds predominantly through an indirect oxidation pathway involving reactive oxygen species (•OH and $O_2^{\bullet-}$) generated at vanadium-ZrO_2 interfaces. These findings establish V–ZrO_2 as a promising, efficient, and visible-light-responsive photocatalyst for dye-contaminated wastewater treatment. Further studies on catalyst recyclability, stability, and mineralization are recommended to support large-scale environmental applications.

Acknowledgments

This manuscript has not been published previously is not under consideration elsewhere, has been approved by all authors and responsible authorities where the work was carried out, and will not be published elsewhere in the same form without the copyright holder's consent.

Data Availability Statement
All data generated or analyzed during this study are included in this published article.

Funding
No funding was received to assist with the preparation or execution of this study.

Competing Interests
The authors declare that they have no known competing financial interests or personal relationships that could have appeared to influence the work reported in this paper.

References

[1] M. Jain, S.A. Khan, K. Sharma, P.R. Jadhao, K.K. Pant, Z.M. Ziora, M.A. Blaskovich, Current perspective of innovative strategies for bioremediation of organic pollutants from wastewater, Bioresour. Technol. 344 (2022) 126305. https://doi.org/10.1016/j.biortech.2021.126305

[2] P.O. Oladoye, T.O. Ajiboye, E.O. Omotola, O.J. Oyewola, Methylene blue dye: Toxicity and potential elimination technology from wastewater, Results Eng. 16 (2022) 100678. https://doi.org/10.1016/j.rineng.2022.100678

[3] J. Abdi, M. Vossoughi, N.M. Mahmoodi, I. Alemzadeh, Synthesis of metal-organic framework hybrid nanocomposites based on GO and CNT with high adsorption capacity for dye removal, Chem. Eng. J. 326 (2017) 1145–1158. https://doi.org/10.1016/j.cej.2017.06.054

[4] V. Katheresan, J. Kansedo, S.Y. Lau, Efficiency of various recent wastewater dye removal methods: A review, J. Environ. Chem. Eng. 6 (2018) 4676–4697. https://doi.org/10.1016/j.jece.2018.06.060

[5] S.I. Sinar Mashuri, M.L. Ibrahim, M.F. Kasim, M.S. Mastuli, U. Rashid, A.H. Abdullah, A. Islam, N. Asikin Mijan, Y.H. Tan, N.

Mansir, Photocatalysis for organic wastewater treatment: From the basis to current challenges for society, Catalysts 10 (2020) 1260.
https://doi.org/10.3390/catal10111260

[6] D. Chen, Y. Cheng, N. Zhou, P. Chen, Y. Wang, K. Li, S. Huo, P. Cheng, P. Peng, R. Zhang, Photocatalytic degradation of organic pollutants using TiO2-based photocatalysts: A review, J. Clean. Prod. 268 (2020) 121725.
https://doi.org/10.1016/j.jclepro.2020.121725

[7] S. Mehra, M. Singh, P. Chadha, Adverse impact of textile dyes on the aquatic environment as well as on human beings, Toxicol. Int. 28 (2021) 165–176.
https://doi.org/10.18311/ti/2021/v28i2/26798

[8] J. Yadav, O. Sahu, Malachite green dye purification from effluent using synthesized ceramic clay: Characterisation; optimization and scale up, Ceram. Int. 49 (2023) 24831–24851.
https://doi.org/10.1016/j.ceramint.2023.05.010

[9] J. Yadav, K. Qanungo, A review: on malachite green; synthesis, uses and toxic effects, AIP Conf. Proc. 2535 (2023) 030020.
https://doi.org/10.1063/5.0111400

[10] J. Sharma, S. Sharma, V. Soni, Toxicity of malachite green on plants and its phytoremediation: a review, Reg. Stud. Mar. Sci. 62 (2023) 102911.
https://doi.org/10.1016/j.rsma.2023.102911

[11] R. Hasan, M.M. Hasan, J.H. Shathi, E. Tamam, A.E. Ahmed, A. Haque, Z. Rahmann, M.T. Islam, M.A. Reza, M.S. Biswas, Toxic effects of malachite green on plant and animal models: A study on root growth inhibition, hematological changes, histopathology, and molecular analysis, Toxicol. Lett. 409 (2025) 61–73.
https://doi.org/10.1016/j.toxlet.2025.05.003

[12] Y. Zheng, G. Luo, G. Chen, R. Jiang, G. Ouyang, Solar-driven degradation of malachite green by photoenzyme: Mechanisms and sustainable water treatment, J. Clean. Prod. 501 (2025) 145335.
https://doi.org/10.1016/j.jclepro.2025.145335

[13] M.A. Hoque, M.I. Guzman, Photocatalytic activity: experimental features to report in heterogeneous photocatalysis, Materials 11 (2018) 1990.
https://doi.org/10.3390/ma11101990

[14] K. Mhalshekar, S. Selvam, A. Sahoo, M.P. Illa, M. Gaydhane, S. Sontakke, Efficient Photocatalytic Degradation of Malachite Green and Cr (VI) Using Co-MOF and Bacterial Cellulose@ Co-MOF Biocomposite: A Green Approach, ACS Omega 10 (2025) 45965–45981.
https://doi.org/10.1021/acsomega.5c06750

[15] S.S. Batool, R. Saleem, R.R.M. Khan, Z. Saeed, M. Pervaiz, M. Summer, Enhancing photocatalytic performance of zirconia-based nanoparticles: A comprehensive review of factors, doping strategies, and mechanisms, Mater. Sci. Semicond. Process. 178 (2024) 108419.
https://doi.org/10.1016/j.mssp.2024.108419

[16] M.A. Wahba, S.M. Yakout, Innovative visible light photocatalytic activity for V-doped ZrO2 structure: optical, morphological, and magnetic properties, J. Sol-Gel Sci. Technol. 92 (2019) 628–640.
https://doi.org/10.1007/s10971-019-05103-2

[17] P. Čičmanec, Y. Ganjkhanlou, J. Kotera, J.M. Hidalgo, Z. Tišler, R. Bulánek, The effect of vanadium content and speciation on the activity of VOx/ZrO2 catalysts in the conversion of ethanol to acetaldehyde, Appl. Catal. A Gen. 564 (2018) 208–217.
https://doi.org/10.1016/j.apcata.2018.07.040

[18] I. Apostolova, A. Apostolov, J. Wesselinowa, Band gap tuning in transition metal and rare-earth-ion-doped TiO2, CeO2, and SnO2 nanoparticles, Nanomaterials 13 (2022) 145.
https://doi.org/10.3390/nano13010145

[19] M. Rezaei, E. Heydari-Bafrooei, A.A. Ensafi, Fabrication of Z-scheme CdTe/CaTiO3-x perovskite heterostructure with enhanced photocatalytic activity, J. Alloys Compd. (2025) 181214.
https://doi.org/10.1016/j.jallcom.2025.181214

[20] E. Heydari-Bafrooei, M. Sabet, Z. Alizadeh, R. Ghazanfarpour, M.H. Moazzen, M. Rezaei, S.S. Varnoosfaderani, M. Ahmadi, Effect of Al and Zn impurities on the electrocatalytic activity of Nb2O5 toward hydrogen evolution reaction, Mater. Chem. Phys. 332 (2025) 130254.
https://doi.org/10.1016/j.matchemphys.2024.130254

[21] M. Rezaei, A. Nezamzadeh-Ejhieh, A.R. Massah, A comprehensive review on the boosted effects of anion vacancy in the photocatalytic solar water splitting: focus on sulfur vacancy, Energy Fuels 38 (2024) 7637–7664.
https://doi.org/10.1021/acs.energyfuels.4c00325

[22] M. Rezaei, A.A. Ensafi, E. Heydari-Bafrooei, MoS2/SrTiO3-x perovskite heterostructure: Fabrication, characterization, and comprehensive photodegradation study towards Rhodamine B, Colloids Surf. A Physicochem. Eng. Aspects 708 (2025) 135993.
https://doi.org/10.1016/j.colsurfa.2024.135993

[23] S. Samantaray, B. Mishra, D. Pradhan, G. Hota, Solution combustion synthesis and physicochemical characterization of ZrO2–MoO3 nanocomposite oxides prepared using different fuels, Ceram. Int. 37 (2011) 3101–3108.
https://doi.org/10.1016/j.ceramint.2011.05.047

[24] A. Adamski, Z. Sojka, K. Dyrek, M. Che, An XRD and ESR study of V2O5/ZrO2 catalysts: influence of the phase transitions of ZrO2 on the migration of V4+ ions into zirconia., Solid State Ion. 117 (1999) 113–122.
https://doi.org/10.1016/S0167-2738(98)00254-9

[25] S. Tibebu, M.A. Gnaro, A.M. Kebede, A.A. Ammona, T. Sime, S. Ayalneh, M.A. Feyisa, M. Jabli, Efficient photocatalytic degradation of methylene blue using Arundo donax biochar/graphitic carbon nitride composite, Results Eng. (2025) 108143.
https://doi.org/10.1016/j.rineng.2025.108143

[26] I.A. Amar, A.A. Nouh, A.M. Aljarani, S.S. Shamsi, K.S. Ghosh, A. Hosseini-Bandegharaei, Surfactant-Assisted Co-Precipitation Synthesis of Zn-doped Tin Ferrite for Methylene Blue and Congo Red Dyes Photodegradation and Phytotoxicity Studies, Chem. Afr. (2025) 1–34.
https://doi.org/10.1007/s42250-025-01472-0

[27] M. Kosmulski, The pH dependent surface charging and points of zero charge. X. Update, Adv. Colloid Interface Sci. 319 (2023) 102973.
https://doi.org/10.1016/j.cis.2023.102973

[28] F. Azeez, E. Al-Hetlani, M. Arafa, Y. Abdelmonem, A.A. Nazeer, M.O. Amin, M. Madkour, The effect of surface charge on photocatalytic degradation of methylene blue dye using chargeable titania nanoparticles, Sci. Rep. 8 (2018) 1–9.
https://doi.org/10.1038/s41598-018-25673-5

[29] I.G. Alhindawy, K. Mahmoud, Engineered zirconia nanomaterials for circular environmental and nuclear applications: dual-function design for photocatalytic pollutant degradation and gamma-ray shielding, Adv. Compos. Hybrid Mater. 8 (2025) 1–25.
https://doi.org/10.1007/s42114-025-01379-x

[30] S. Ojala, T. Laitinen, S. Leneuf de Neufville, M. Honkanen, M. Vippola, M. Huuhtanen, R.L. Keiski, Vanadia–zirconia and vanadia–hafnia catalysts for utilization of volatile organic compound emissions, Materials 14 (2021) 5265. https://doi.org/10.3390/ma14185265

[31] A. Moshfegh, A. Ignatiev, Formation and characterization of thin film vanadium oxides: Auger electron spectroscopy, X-ray photoelectron spectroscopy, X-ray diffraction, scanning electron microscopy, and optical reflectance studies, Thin Solid Films 198 (1991) 251–268. https://doi.org/10.1016/0040-6090(91)90344-W

[32] S. Chen, F. Ma, A. Xu, L. Wang, F. Chen, W. Lu, Study on the structure, acidic properties of V–Zr nanocrystal catalysts in oxidative dehydrogenation of propane, Appl. Surf. Sci. 289 (2014) 316–325. https://doi.org/10.1016/j.apsusc.2013.10.158

[33] D. Gazzoli, S. De Rossi, G. Ferraris, G. Mattei, R. Spinicci, M. Valigi, Bulk and surface structures of V2O5/ZrO2 catalysts for n-butane oxidative dehydrogenation, J. Mol. Catal. A Chem. 310 (2009) 17–23. https://doi.org/10.1016/j.molcata.2009.05.014

[34] N. Horti, M. Kamatagi, S. Nataraj, M. Wari, S. Inamdar, Structural and optical properties of zirconium oxide (ZrO2) nanoparticles: effect of calcination temperature, Nano Express 1 (2020) 010022. https://doi.org/10.1088/2632-959X/ab8684

[35] F. Ren, S. Ishida, N. Takeuchi, Color and Vanadium Valency in V-Doped ZrO2, J. Am. Ceram. Soc. 76 (1993) 1825–1831. https://doi.org/10.1111/j.1151-2916.1993.tb06654.x

[36] J.R. Sohn, S.G. Cho, Y.I. Pae, S. Hayashi, Characterization of vanadium oxide–zirconia catalyst, J. Catal. 159 (1996) 170–177. https://doi.org/10.1006/jcat.1996.0076

[37] Y. Luo, Y. Wu, Defect engineering of nanomaterials for catalysis, Nanomaterials 13 (2023) 1116. https://doi.org/10.3390/nano13061116

[38] B.D. Cullity, R. Smoluchowski, Elements of X-ray Diffraction, Phys. Today 10 (1957) 50. https://doi.org/10.1021/ja01564a077

[39] A. Bumajdad, A.A. Nazeer, F. Al Sagheer, S. Nahar, M.I. Zaki, Controlled synthesis of ZrO2 nanoparticles with tailored size, morphology and crystal phases via organic/inorganic hybrid films, Sci. Rep. 8 (2018) 3695. https://doi.org/10.1038/s41598-018-22088-0

[40] M. Petriceanu, F.G. Ioniță, R.R. Piticescu, A.I. Nicoară, A.C. Matei, M.A. Ioța, I.A. Tudor, Ș. Caramarin, C.F. Ciobota, Effect of Doping ZrO2 on Structural and Thermal Properties, Inorganics 12 (2024) 290. https://doi.org/10.3390/inorganics12110290

[41] Y. Kera, S. Teratani, K. Hirota, Infrared Spectra of Surface V= O Bond of Vanadium Pentoxide, Bull. Chem. Soc. Jpn. 40 (1967) 2458. https://doi.org/10.1246/bcsj.40.2458

[42] A. Teimouri, B. Najari, A.N. Chermahini, H. Salavati, M. Fazel-Najafabadi, Characterization and catalytic properties of molybdenum oxide catalysts supported on ZrO2–γ-Al2O3 for ammoxidation of toluene, RSC Adv. 4 (2014) 37679–37686. https://doi.org/10.1039/C4RA07435A

[43] M. Patel, S. Mishra, R. Verma, D. Shikha, Synthesis of ZnO and CuO nanoparticles via Sol gel method and its characterization by using various technique, Discov. Mater. 2 (2022) 1. https://doi.org/10.1007/s43939-022-00022-6

[44] D. Gazzoli, S. De Rossi, G. Ferraris, M. Valigi, L. Ferrari, S. Selci, Morphological and textural characterization of vanadium oxide supported on zirconia by ionic exchange, Appl. Surf. Sci. 255 (2008) 2012–2019. https://doi.org/10.1016/j.apsusc.2008.06.139

[45] S.R. Teeparthi, E.W. Awin, R. Kumar, Dominating role of crystal structure over defect chemistry in black and white zirconia on visible light photocatalytic activity, Sci. Rep. 8 (2018) 5541. https://doi.org/10.1038/s41598-018-23648-0

[46] M. Kantcheva, Spectroscopic characterization of VOx/ZrO2 catalysts prepared using vanadium (V) oxo complexes, Solid State Ion. 141 (2001) 487–492. https://doi.org/10.1016/S0167-2738(01)00793-7

[47] M. Rezaei, A. Nezamzadeh-Ejhieh, The ZnO-NiO nano-composite: a brief characterization, kinetic and thermodynamic study and study the Arrhenius model on the sulfasalazine photodegradation, Int. J. Hydrogen Energy 45 (2020) 24749–24764. https://doi.org/10.1016/j.ijhydene.2020.06.258

[48] A.Z. Johannes, R.K. Pingak, M. Bukit, Tauc Plot Software: Calculating energy gap values of organic materials based on Ultraviolet-Visible absorbance spectrum, in: IOP Conf. Ser. Mater. Sci. Eng., IOP Publishing, 2020, pp. 012030.

[49] Z. Xu, N. Zada, F. Habib, H. Ullah, K. Hussain, N. Ullah, M. Bibi, M. Bibi, H. Ghani, S. Khan, Enhanced photocatalytic degradation of malachite green dye using silver–manganese oxide nanoparticles, Molecules 28 (2023) 6241. https://doi.org/10.3390/molecules28176241

[50] Y. Chen, M. Cai, J. Li, W. Zhang, Study on Photocatalytic Performance of Bi2O3-TiO2/Powdered Activated Carbon Composite Catalyst for Malachite Green Degradation, Water 17 (2025) 1452. https://doi.org/10.3390/w17101452

[51] M.F. Elkady, H.S. Hassan, Photocatalytic degradation of malachite green dye from aqueous solution using environmentally compatible Ag/ZnO polymeric nanofibers, Polymers 13 (2021) 2033. https://doi.org/10.3390/polym13132033

[52] P. Bansal, N. Bhullar, D. Sud, Studies on photodegradation of malachite green using TiO2/ZnO photocatalyst, Desalin. Water Treat. 12 (2009) 108–113. https://doi.org/10.5004/dwt.2009.944

[53] K. Saeed, M. Sadiq, I. Khan, S. Ullah, N. Ali, A. Khan, Synthesis, characterization, and photocatalytic application of Pd/ZrO2 and Pt/ZrO2, Appl. Water Sci. 8 (2018) 60. https://doi.org/10.1007/s13201-018-0709-7

[54] F. Boran, M. Okutan, Synthesis optimization of ZrO2 nanostructures for photocatalytic applications, Turk. J. Chem. 47 (2023) 448–464. https://doi.org/10.55730/1300-0527.3551

[55] C. Mita, N. Cornei, M. Frenti, G. Bulai, M. Dobromir, V. Tiron, A.S. Doroshkevich, D. Mardare, Photocatalytic Activity of N-Doped ZrO2 Thin Films Determined by Direct and Indirect Irradiation, Materials 16 (2023) 5901. https://doi.org/10.3390/ma16175901

[56] M.H. Zare, A. Mehrabani-Zeinabad, Photocatalytic activity of ZrO2/TiO2/Fe3O4 ternary nanocomposite for the degradation of naproxen: characterization and optimization using response surface methodology, Sci. Rep. 12 (2022) 10388. https://doi.org/10.1038/s41598-022-14674-0

[57] S. Jabeen, M. Sufaid Khan, R. Khattak, I. Zekker, J. Burlakovs, S.S.d. Rubin, M.M. Ghangrekar, A. Kallistova, N. Pimenov, M. Zahoor, Palladium-supported zirconia-based catalytic degradation of rhodamine-b dye from wastewater, Water 13 (2021) 1522. https://doi.org/10.3390/w13111522

[58] F. Alresheedi, Hydrothermal sol–gel synthesis of zirconium dioxide (ZrO2) nanoparticles for enhanced degradation of Congo Red, Results Phys. 79 (2025) 108521. https://doi.org/10.1016/j.rinp.2025.108521

[59] A. Ajmal, I. Majeed, R.N. Malik, H. Idriss, M.A. Nadeem, Principles and mechanisms of photocatalytic dye degradation on TiO2 based photocatalysts: a comparative overview, RSC Adv. 4 (2014) 37003–37026. https://doi.org/10.1039/C4RA06658H

[60] Y. Khan, H. Sadia, S.Z. Ali Shah, M.N. Khan, A.A. Shah, N. Ullah, M.F. Ullah, H. Bibi, O.T. Bafakeeh, N.B. Khedher, Classification, synthetic, and characterization approaches to nanoparticles, and their applications in various fields of nanotechnology: a review, Catalysts 12 (2022) 1386. https://doi.org/10.3390/catal12111386

[61] M.K.H.M. Nazri, N. Sapawe, A short review on photocatalytic toward dye degradation, Mater. Today Proc. 31 (2020) A42–A47. https://doi.org/10.1016/j.matpr.2020.10.967

[62] V. Selvaraj, T.S. Karthika, C. Mansiya, M. Alagar, An over review on recently developed techniques, mechanisms and intermediate involved in the advanced azo dye degradation for industrial applications, J. Mol. Struct. 1224 (2021) 129195. https://doi.org/10.1016/j.molstruc.2020.129195

[63] W. Fang, J. Yan, Z. Wei, J. Liu, W. Guo, Z. Jiang, W. Shangguan, Account of doping photocatalyst for water splitting, Chin. J. Catal. 60 (2024) 1–24. https://doi.org/10.1016/S1872-2067(23)64637-6